


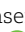
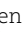

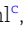

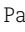
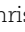
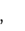


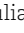

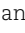




3D multiscale characterization of the human placenta: Bridging anatomy and histology by X-ray phase-contrast tomography

Jakob Reichmann ^a, Anne Schnurpfeil ^a, Sylvia Mittelstädt ^b, Patrick Moller Jensen ^c, Vedrana Andersen Dahl ^c, Anders Bjorholm Dahl ^c, Carina Weide ^b, Eva von Campenhausen ^a, Hector Dejea ^d, Paul Tafforeau ^d, Christopher Werlein ^e, Danny Jonigk ^{f,g}, Maximilian Ackermann ^h, Klaus Engel ⁱ, Julia Gallwas ^b, Alexander Dietz ^j, Mir Fuad Hasanov ^b and Tim Salditt ^{b,a,*}

^aInstitute for X-ray Physics, University of Göttingen, Göttingen 37077, Germany

^bDepartment of Gynecology and Obstetrics, University Medical Center Göttingen, Göttingen 37973, Germany

^cDTU Compute, Technical University of Denmark, Kongens Lyngby 2800, Denmark

^dESRF, The European Synchrotron Radiation Facility, Grenoble 38000, France

^eInstitute of Pathology, Hannover Medical School, Hanover 30625, Germany

^fInstitute of Pathology, RWTH Aachen Medical Faculty, Aachen 52074, Germany

^gGerman Center for Lung Research (DZL), BREATH, Hanover 30625, Germany

^hInstitute of Pathology and Department of Molecular Pathology, Helios University Clinic Wuppertal, University of Witten/Herdecke, Wuppertal 42283, Germany

ⁱSiemens Healthineers AG, Erlangen 91052, Germany

^jInstitute of Pathology, University Medical Center Göttingen, Göttingen 37075, Germany

*To whom correspondence should be addressed: Email: tsalditt@gwdg.de

Edited By Offer Erez

Abstract

The human placenta exhibits a complex three-dimensional (3D) structure with a interpenetrating vascular tree and large internal interfacial area. In a unique and yet insufficiently explored way, this parenchymal structure enables its multiple functions as a respiratory, renal, and gastrointestinal multiorgan. The histopathological states are highly correlated with complications and health issues of mother, and fetus or newborn. Macroscopic and microscopic examination has so far been challenging to reconcile on the entire organ. Here we show that anatomical and histological scales can be bridged with the advent of hierarchical phase-contrast tomography and highly brilliant synchrotron radiation. To this end, we are exploiting the new capabilities offered by the BM18 beamline at ESRF, Grenoble for whole organ as well as the coherence beamline P10 at DESY, Hamburg for high-resolution, creating unique multiscale datasets. We also show that within certain limits, translation to μ CT instrumentation for 3D placenta examination becomes possible based on advanced preparation and CT protocols, while segmentation of the datasets by machine learning now remains the biggest challenge.

Keywords: placenta, multiscale imaging, tissue morphology, X-ray phase-contrast imaging, intact organ imaging

Significance Statement

Our study harnesses cutting-edge synchrotron and laboratory X-ray imaging techniques, to bridge anatomical and histological scales and generate high-resolution, multiscale datasets of an intact placenta. The results leverage XPCT as a suitable technique to advance the understanding of placental development and function, and may lead to diagnostic tools for predicting and preventing pregnancy complications.

Introduction

With its intricate feto-placental vessel network confined within villous trees (1), the placenta is an excellent example of how the three-dimensional (3D) architecture of tissue and vasculature enables its function. Here, the proximity between maternal and fetal blood vessels is essential to provide sufficient nutrients and oxygen to the

fetus, while removing waste products and carbon dioxide. In clinical practice, placental examination can provide important information about maternal diseases, the cause of preterm delivery, fetal growth restriction, or fetal neurodevelopmental damage (2). Despite the information which can be gained from it, the organ is however frequently overlooked and discarded without proper examination.

Competing Interest: The authors declare no competing interests.

Received: August 7, 2024. **Accepted:** November 28, 2024

© The Author(s) 2025. Published by Oxford University Press on behalf of National Academy of Sciences. This is an Open Access article distributed under the terms of the Creative Commons Attribution-NonCommercial License (<https://creativecommons.org/licenses/by-nc/4.0/>), which permits non-commercial re-use, distribution, and reproduction in any medium, provided the original work is properly cited. For commercial re-use, please contact reprints@oup.com for reprints and translation rights for reprints. All other permissions can be obtained through our RightsLink service via the Permissions link on the article page on our site—for further information please contact journals.permissions@oup.com.

As a result, many aspects of placenta morphology, cytoarchitecture, and medically relevant abnormalities remain elusive, and with limited data available. Beyond the current indications and clinical recommendations, a significant potential for future advanced diagnostics can be assumed, and a not yet fully exploited source of information for the etiology of maternal and fetal disorders. Given the fact that the organ is easily available, and that its examination is not associated with any risks for mother or baby, large cohorts can be achieved, with corresponding benefits for the training of machine learning models and artificial intelligence. While macroscopic and microscopic assessment of the placenta can in principle be combined, one must take note, however, that microscopic pathological investigation is extremely laborious if larger volumes of the placenta have to be sampled. For studies of placental tissue organization on multiple scales both in view of general physiology and pathological manifestations, a multiscale 3D imaging technique is required which resolves tissue morphology and the vascular network while providing a large field of view.

Different imaging modalities are available for the investigation at tissue and organ level, providing comprehensive insight into physiological and pathophysiological states. Magnetic resonance imaging (MRI), including volumetric MRI, diffusion tensor imaging (DTI), and functional MRI (fMRI), can inform us about placenta morphology or functional connectivity alterations (3). On the microscopic scale, cellular and subcellular resolution is still primarily provided by optical microscopy performed on tissue sections, and can now be combined with a plethora of specific molecular labels. Based on histological sections, microscopic inspection of the cytoarchitecture still remains the gold standard of histology and pathohistology.

In recent years, propagation-based X-ray phase-contrast tomography (XPCT) emerged as a promising technique for tissue imaging, offering a unique potential to extend histology and pathohistology to the third dimension, covering multiple length scales from whole organs (4–6) to sub-100 nm resolution (7, 8). Importantly, XPCT provides a scalable and isotropic resolution without destructive slicing of the specimen and quantitative density-based contrast (9–17). At the same time, XPCT is extremely flexible concerning the sample environment (18–20). Recently, complementing histological investigation, XPCT was used to study murine (21) and human placenta vasculature and tissue architecture (22–24). In previous studies, however, tissue samples were either extracted from the organ, or contrast was too low to study tissue morphology and vasculature, unless involved contrast enhancement by staining agents or resin filling was employed.

In this work, we demonstrate the unprecedented capabilities emerging from recent advances in whole organ XPCT, also denoted as hierarchical phase-contrast tomography (HiP-CT) (4), as implemented at the novel synchrotron beamline BM18 (ESRF, Grenoble, France). Entire intact, non-stained, human placentas can be imaged in 3D at sub 20 μm voxel size and a superior contrast, allowing to study the vascular network and tissue morphology. Structures of interest such as infarctious regions, fibrin depositions, and intervillous thrombi can be detected in the entire organ and characterized in 3D. We present different approaches for image segmentation, and for the translation of HiP-CT to a laboratory setup. We then extend whole organ 3D imaging by subsequent, targeted extraction of biopsies from the organ, which are then studied at submicron voxel sizes at the P10 coherent imaging beamline (PETRA III, Hamburg, Germany). In this way, we contribute comprehensive 3D datasets for a placenta atlas with unprecedented contrast and resolution.

The manuscript is organized as follows: following this introduction, methods of sample preparation and image acquisition are detailed, as well as the analysis workflow including the data processing methods and the segmentation and visualization techniques. Subsequently, the results of the hierarchical imaging configuration are presented together with different segmentation approaches. Then, results obtained on whole organs at a laboratory setup and of placenta tissue biopsies imaged at high resolution are showcased. The manuscript concludes with a discussion and summary of the results together with an outlook for future studies.

Methods

All experiments were approved by the UMG (Universitätsmedizin Göttingen) ethics commission (permit number: 21/12/22), and samples were de-identified prior to use in the study.

Sample preparation

Figure 1a schematically illustrates the sample preparation procedure. Placenta samples were either embedded as a whole or cut into smaller pieces. In total, five intact organs were prepared for the scans, following the protocol proposed by Brunet et al. (18). After extraction, the samples were immediately immersed in formalin (4.5% FA, PBS buffered [Histofix, Carl Roth, Karlsruhe]) and cross-fixed for 6 to 7 days. Afterwards, the samples were dehydrated in solutions with ascending (not denatured) ethanol (EtOH) concentrations (50%, 60%, and 70%, 3 to 4 days each). Agar was cooked, cut in cubes or shredded and subsequently put in a 70% EtOH solution. Each placenta was then placed in a plastic jar (Cornucopia Gallon Plastic Jars, BPA free) with a diameter of 14 cm and a height of 26 cm. Agar cubes were placed at the bottom of the jar (until 3–5 cm above bottom). Shredded agarose was added to fill the intermediate empty spaces. Then, the organ was carefully inserted into the container in a vertical position. Simultaneously, shredded agarose was placed in the surrounding space, stabilizing the organ. To make sure the organ did not dry out and to prevent bubble formation, the container was filled up with (70% EtOH) solution every 10 to 15 min. To delay bubble formation (25), the filled jar was then degassed (down to 80 mbar), the solution was pumped out again, more shredded agarose inserted and re-densified. This procedure was iterated until the organ was entirely covered in agarose and fully stabilized. Finally, agarose cubes were added on top of the embedded organ until the jar was fully filled and, after repeated degassing, the jar was sealed. Smaller samples were placed in jars with smaller diameter (9 cm) or large Falcon tubes (3 cm in diameter, 50 mL volume) and sealed after repeated degassing. For reference (empty beam) images, identical jars/tubes were filled with a 70% EtOH solution to serve as reference. Note that as a central advantage of HiP-CT empty (jar) images account for the attenuation caused by the embedding media in the sample jar, providing an improved reference in view of beam hardening, and also higher dynamic range. This procedure was used for all EtOH embedded samples shown in the manuscript (except BM18-HR setup, see Table 1).

For scans recorded at the GINIX-endstation (Table 1: P10-PB) at P10 (PETRA III), 3 mm biopsies were punched out of the fetal side of the placenta or punched out of the center with a cylindrical rod. After a dehydration series, the samples were placed in 4.3 mm wide glass capillaries filled with 70% EtOH and locally fixed with shredded agarose. Here as well, the empty beam, projections

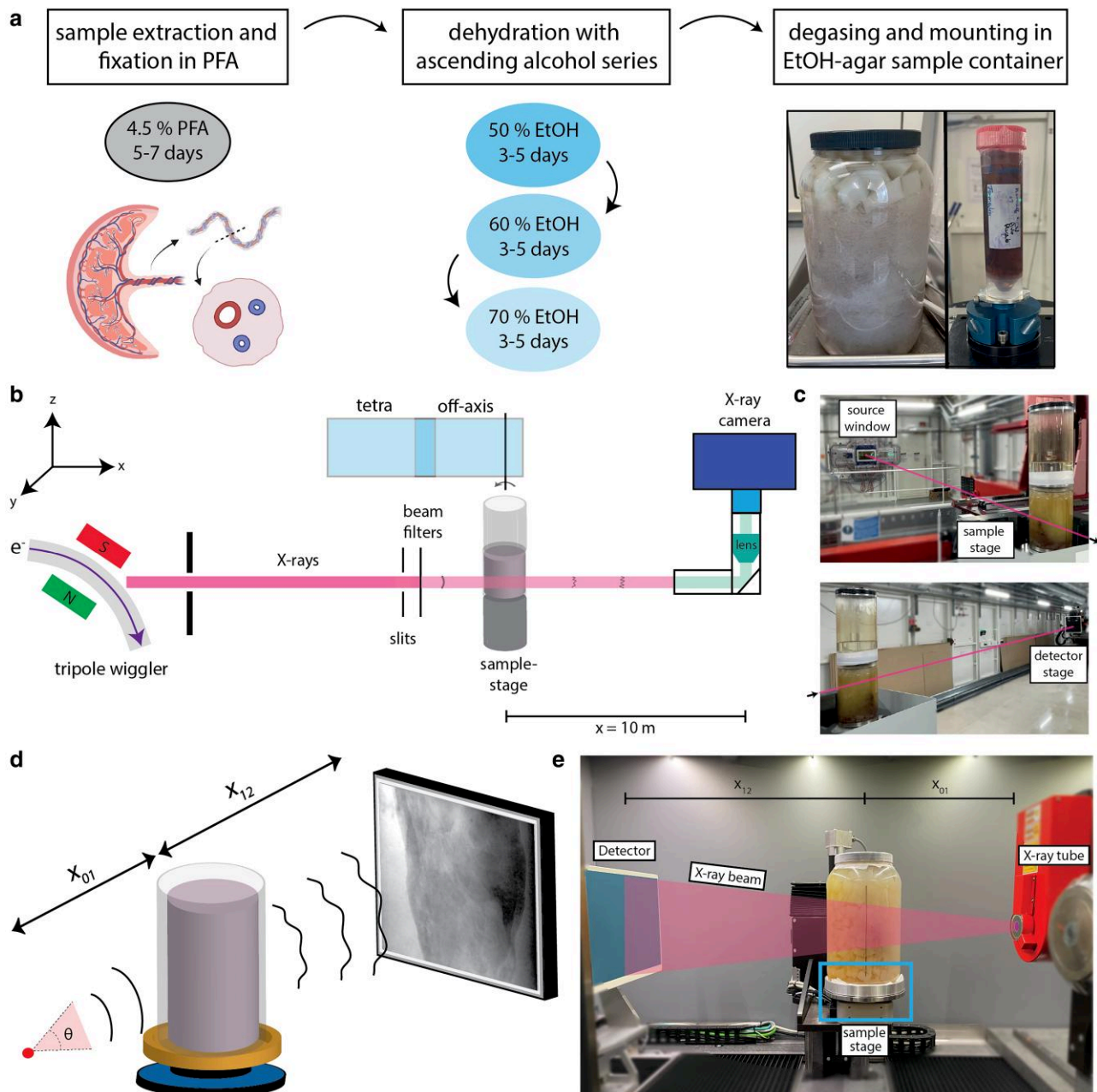


Fig. 1. Schematic of experimental procedure and data acquisition. a) Illustration of sample preparation starting with sample extraction and fixation in 4.5% PFA, followed by dehydration with ascending alcohol series and completed by degassing and mounting of the sample in an EtOH-agar-filled sample container. After data acquisition (see [b]–[e]), features of interest are segmented, rendered, and quantitatively assessed. b) Illustration of the experimental setup at the BM18 beamline (ESRF, Grenoble). A tripole wiggler is used to generate X-rays which are attenuated by the sample and are recorded by an X-ray camera. c) Photograph of the experimental setup illustrated in (b) (top: source direction, bottom: detector direction). d) Cone beam geometry for X-ray data acquisition at an in-house μ /nano-CT setup (RX Solutions, France). e) Photograph of the in-house experimental setup with a nano-focus source, flat panel detector and the sample placed on a rotation stage.

were acquired inside the same capillary above the sample with only the 70% EtOH solution present.

Experimental setups

For this experiment, data were collected at three different sources/instruments and four different setups: a laboratory μ -CT system (EasyTom, RX Solutions, Chavanod), in two configurations at the BM18 synchrotron beamline dedicated for hierarchical full-field phase-contrast tomography of large samples (ESRF, Grenoble), and at the GINIX instrument of the P10 beamline at

the PETRA III storage ring (DESY, Hamburg). For all recording of intact organs, the HiP-CT protocol (4) was used.

HiP-CT beamline (BM18)

The BM18 beamline uses a tripole wiggler source without any additional crystal monochromator. The broad polychromatic energy spectrum can be further tuned by a set of filters, with a typical range between 50 and 320 keV. The beam size at sample level can cover a FOV of up to $350.0 \times 17.0 \text{ mm}^2$ (adjustable with a slit system), allowing to image larger organs at multiple scales

Table 1. Parameters for the synchrotron setups BM18 (-T: whole organ acquisition, -HR: high-resolution acquisition with extracted tissue sample, ESRF, Grenoble) and P10-PB (parallel beam setup, GINIX, PETRA III, Hamburg) as well as the laboratory setup (μ CT, EasyTom, RX solutions, Chavanod). The FOV is given for a single radiograph, for the BM18-T setup the lateral stitching resulted in an FOV of 150.2 mm \times 8.06 mm. The total scan time is calculated for 28 z-positions for BM18-T, 10 z-positions for BM18-HR, and for a single tomogram with flat and dark fields for P10-PB.

Tube Voltage/(avg) Energy	BM18-T 92 keV	BM18-HR 68.5 keV	P10-PB 15 keV	μ CT 150 kV
τ (s)	0.013	0.02	0.035	1.43
X_{01}	177.6 m	177.6 m	–	312 mm
X_{12}	10 m	2.4 m	22 mm	480 mm
pX_{eff} (μ m)	19.19	3.164	0.65	50
FOV (H \times V) (mm ²)	48.5 \times 8.06	16 \times 4.43	1.6 \times 1.4	91 \times 67.5
No. of projections	12,000	8,000	3,000	1,440
No. accumulations	3	3	0	20
Tot. scan time	~9 h	~106 min	75 s	~20 h
Total dose (kGy)	168	61.92	–	–

(depending on slits and detectors), with a maximum propagation distance of 38 m, high-throughput and unprecedented contrast and resolution at the whole organ scale.

For the experiments presented in this work, two different acquisition modes were implemented. In the first configuration, the so-called tetra acquisition setup (BM18-T, part of the so-called HiP-CT protocol (4)) was implemented (see Fig. 1b,c). The beam was attenuated using Al_2O_3 (7 mm thickness), Molybdenum (0.21 mm thickness), and a glassy carbon block (30 mm thickness), resulting in an average energy of 92 keV. Vertical slits were used to crop the beam height to 8.06 mm. The beam propagated through air (10 m propagation distance) and was recorded by an indirect detection systems, which could be varied as required. For the BM18-T configuration of whole organ recordings, we used a custom built detector equipped with a LuAG:Ce scintillator (2 mm thickness, Crytur, Czech Republic), a dzoom optic, and an Iris 15 sCMOS detector (Teledyne Photometrics, USA) with 5,056 (H) \times 2,960 (V) pixels. Cropping the detector chip and constraining the FOV with vertical slits resulted in an effective detector size of 2,528 (H) \times 420 (V) pixels (48.5 mm (H) \times 8.06 mm (V)). Taking the geometrical zoom into account and after 2 \times 2 binning at the detector, the effective pixel size was 19.19 μ m. In total, 12,000 projections were recorded over 360° with a per-frame exposure time of 13 ms. Three projections were recorded at each angle (with small deviations in angular position due to continuous rotation) and later averaged in order to increase the signal-to-noise ratio. In order to increase the lateral field of view, scans were done in tetra acquisition mode. Here, a central off-axis scan and an annular off-axis scan are laterally stitched together to reach a final lateral field of view of 7,827 pixels (150.2 mm). By moving the sample 7 mm after each scan, 28 tomograms were recorded and vertically stitched to an overall volume height of 19.6 cm with a total scan time of ~9 h.

For the second configuration, here referred to as the BM18 high-resolution setup (BM18-HR), a Al_2O_3 filter (0.5 mm) and 110 mm of glassy carbon blocks were inserted in the beam. A LuAG:Ce 100 μ m scintillator with a zoom optic coupled optically to a sCMOS camera (5,056 (H) \times 2,960 (V) pixel, Iris 15, Teledyne Technologies, Thousand Oaks, USA) with 4.25 μ m physical pixel size resulted in an effective pixel size of 3.164 μ m. Constraining the chip size with vertical slits to 5,056 (H) \times 1,400 (V) pixels resulted in an FOV of 16 mm \times 4.43 mm. As an example, a scan consisting of 10 z-positions (vertical translation of 3.2 mm between each scan) took around 106 min. Here, off-axis scans were acquired (no tetra acquisition) with empty beam images recorded in air, following the standard imaging protocol. Scan parameters are tabulated in Table 1: BM18-HR.

In-house X-ray system

Before recording tomographic scans at the laboratory μ CT-setup (EasyTom, RX Solutions), the reference jar was centered on the sample stage. Then, distance and acquisition settings were selected, and a series of 128 projection images was recorded with a flat panel detector (CsI scintillator) with a physical pixel size of 127 μ m. For each projection angle, several acquisitions were averaged. For the empty beam correction, the reference jar was used (according to HiP-CT, as described in (4)). The configuration is depicted in Fig. 1d,e, and all relevant scan parameters are listed in Table 1: μ CT.

Nano-imaging setup (P10)

The parallel beam configuration at the GINIX endstation (P10, DESY, Hamburg) allows for a field of view (FOV) of approximately 1.4 \times 1.6 mm, probed at 0.65 μ m pixel size with highly coherent monochromatic radiation (Si(111) channel-cut monochromator) in continuous rotation mode, resulting in an overall scan time of approximately 2 min. Single distance tomograms were recorded with 3,000 projections acquired over 360°. A high-resolution detection system was used (Optique Peter, France) with a 50 mm-thick LuAG:Ce scintillator and a 10 \times magnifying microscope objective (26), coupled to a pco.edge 5.5 sCMOS camera (PCO, Germany). The camera performs with a maximum frame rate of 100 Hz, utilizing a rolling shutter and fast scan mode. This detection scheme yielded an effective pixel size of 0.65 μ m, the beam size was adjusted to approximately 2 \times 2 mm using the upstream slit systems. This experimental setup was previously described in (20, 27, 28). Here, a conventional flat field acquisition protocol was applied for FFPE samples while the HiP-CT protocol was applied for liquid embedded samples (see [Sample preparation](#)).

Histological examination

After XPCT-imaging, the paraffin samples were re-embedded in paraffin blocks and 2 μ m thick sections were cut followed by histological staining using Hematoxylin and Eosin (HE) at the Institute of Pathology at Hannover Medical School. Immunohistochemistry for CD31, ready-to-use (clone JC70A, Cell Marque, Rocklin, CA, USA) and CD163, ready-to-use (clone MRQ-26, Cell Marque, Rocklin, CA, USA) were stained on a VENTANA BenchMark ULTRA (Hoffmann-La Roche, Basel, Swiss) platform with the aforementioned dilutions, pretreatment and incubation times according to the manufacturer's advice. Histology slides were scanned using an Aperio CS2 slide Scanner (Leica Biosystems, Nussloch, Germany), and images were acquired using QuPath (29).

Segmentation and visualization of the vascular tree

For all imaging setups, phase reconstruction algorithms were used to retrieve the phase information encoded in the recorded intensity (BM18, μ CT: Paganin-based phase retrieval; P10-PB: CTF-based phase retrieval). After tomographic reconstruction of the recorded, phase-retrieved, projections and visual inspection by practising pathologists/gynecologists, the vasculature was segmented using seeded watershed algorithms, deep learning-based techniques, or simple thresholding. For volumetric data annotation, webknossos (Scalable minds UG, Potsdam, Germany (30)) and micro-sam (31, 32) were used. Subsequently, rendering software such as NVIDIA IndeX (NVIDIA, Santa Clara, USA), Avizo 3D (Thermo Fisher Scientific, Waltham, USA), Cinematic Anatomy (Siemens Healthineers, Erlangen, Germany), VGSTUDIO MAX (Hexagon, Stockholm, Sweden), and ZEISS arivis (Carl Zeiss AG, Oberkochen, Germany) was used for a three-dimensional visualization of the dataset. For additional post processing such as orthogonal views and maximum intensity projections, the Fiji software was used (33).

Results

Hierarchical whole organ XPCT

Using existing acquisition protocols, the BM18 beamline allows to capture the tissue architecture of an organ on multiple scales with voxel sizes spanning from high-resolution scans with a few micron voxel size to whole organ scans with several tens of micrometers and FOVs sufficient to cover the entire human placenta. Figure 2a showcases such a scan, where the entire organ is covered in a sequential acquisition of 28 scans (translation in z-direction). This enables 3D visualization at the microanatomical and as well as the histological level. Tissue density and morphology, and in particular also the thinning vasculature tree can be assessed quantitatively. The contrast and resolution are sufficient to extract and quantify morphometric parameters such as tissue density variation, or local shape measures based on the structure tensor (20, 27, 34), or other advanced radiomic quantities (35). Notably, coagulated blood in the vascular system as well as calcified vessels results in very strong X-ray absorption, taking the role of an inherent vascular contrast agent. Due to the process of formation, however, the blood clots are not continuous but break apart and are therefore interrupted and occluded vascular regions alternate. This strong variation in contrast makes a segmentation based on conventional techniques such as simple thresholding, watershed or seed/gradient-based segmentation ineffective, requiring advanced deep learning based segmentation methods, e.g. by implementation of a U-Net architecture. This approach is described in more detail further below. The orange box in Fig. 2a shows a subacute intervillous thrombus with its characteristic laminar-structured lesions (lines of Zahn), as previously described in (36) (in more detail shown in Fig. 5c, d). Complementary histopathological investigation show these lesions to consist of thrombocytes and a fibrin network with a large number of erythrocytes (a correlative comparison is presented in Fig. S3). In Fig. 2b, a reconstruction of the umbilical cord is shown, obtained from a high-resolution scan (Table 1: BM18-HR), resolving the umbilical arteries and umbilical vein in great detail together with the mucous connective tissue (Wharton's jelly). Wharton's jelly contains branched fibrocytes (with visible cell nuclei) embedded in a meshwork of collagen and reticulin fibers. Vein and artery walls with their respective layered structure are clearly resolved. Umbilical arteries and umbilical vein are

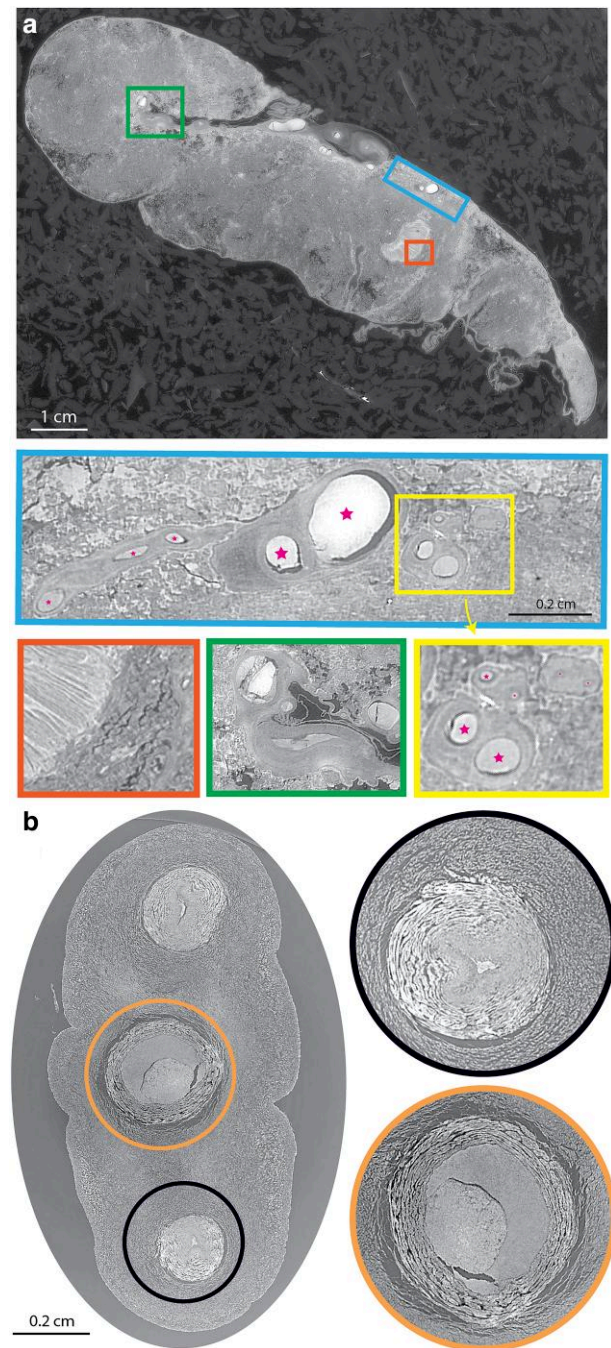


Fig. 2. Physiological placenta recorded at the BM18 beamline using the HiP-CT protocol. a) Tomographic slice through the entire placenta (Table 1: BM18-T) with zoom-in at regions of interest (green, amniotic membrane; orange, infarctious regions; yellow, vasculature). Pink stars represent structures of the vascular network. b) High-resolution scan (Table 1: BM18-HR1) of umbilical cord with zoom-in at umbilical artery (black) and umbilical vein (orange).

segmented and visualized in Fig. 5a, revealing a thickening of the umbilical cord (vascular ectasia). Additional histological sections of the umbilical cord are showcased in Fig. 8c.

In Fig. 3, a tissue sample of approx. 2.5 cm is shown, which was extracted from a SARS-CoV-2-infected placenta. The tissue was scanned using the high-resolution setup (Table 1: BM18-HR) which allows to resolve structures in the terminal villous unit, as well as syncytiotrophoblasts in the endocrine tissue regions

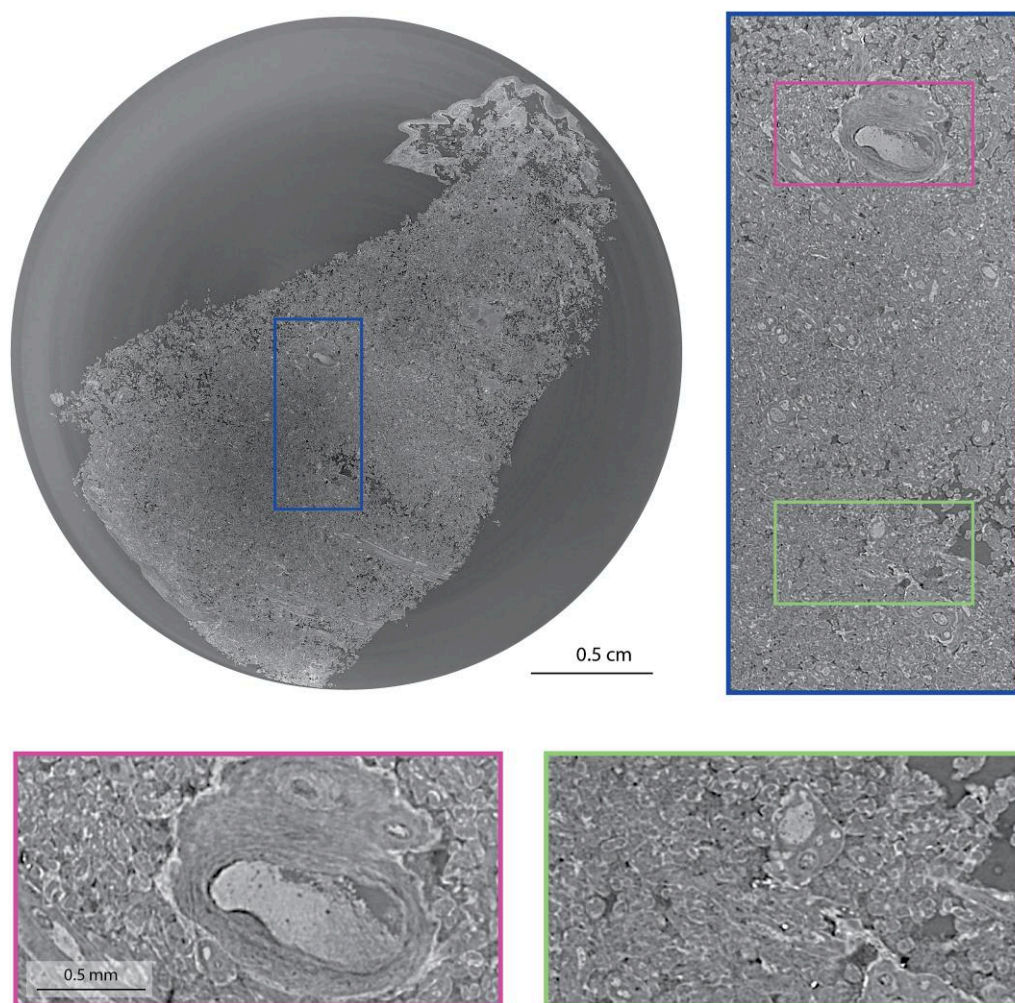


Fig. 3. SARS-CoV-2 infected placenta recorded at BM18 beamline using the conventional imaging protocol (see Table 1: BM18-HR). Zoom-in regions show vessels (purple box, top) and placental tissue cytoarchitecture (green box, bottom). The lighter (denser) interfaces surrounding the terminal villi (zoom-in in the green box) can be associated with the syncytiotrophoblast. The intervillous space appears to be reduced.

of the placenta. The syncytiotrophoblast is the endocrine tissue covering the highly vascularized chorionic villi. Previous histological studies of placentas from SARS-CoV-2 infection fetuses revealed pathologies including chronic histiocytic intervillitis and syncytiotrophoblast necrosis (37, 38). In these cases, the intervillous space seemed compressed and reduced, an observation in line with the morphological appearance in Fig. 3.

Besides virtually slicing the volume and screening for features of interest, 3D visualization is necessary to study the three-dimensionality of the volume in its entirety. Recent major advancements with regard to GPU based rendering and dedicated software packages provide have enabled photo-realistic renderings of the reconstruction volume by using shaders to control lighting, texture, color, and further parameters of 3D models. Figure 4 shows a rendering of a healthy placenta scanned with the BM18-T configuration. The rendering was created by the so-called cinematic volume rendering technology (cVRT) (Siemens Healthineers, Germany), which is based on real-time Monte-Carlo path tracing. The software includes several algorithmic steps such as computation of interpolated density values, density classification, gradient computation, and shading. To this end, CVRT takes into account physical optical effects (absorption, emission, scattering) to simulate a complex interaction of light

with the scanned object. Additionally, complex light effects (shadows, light absorption/scattering, ambient occlusion, and caustic effects) together with classical camera features can be mimicked. This allows to study the detailed surface of the placenta, see for example the fetal side shown in Fig. 4a,d, and also to virtually cut through the organ as in Fig. 4b,c. Tissue heterogeneity can be inspected in certain regions, the vascular tree can be followed from the umbilical cord to tiny capillaries, and specific features of interest can be represented in unprecedented detail. Figure 4e showcases the intricate network of the winding and branching vasculature tree, with the required visual effects achieved by manipulation of the opacity in the histogram. The strong contrast is caused by the clotted blood. Correspondingly, gaps appear where blood is missing. This prevents a segmentation by thresholding gray values, while segmentation of the entire network would be desirable, for quantification purposes. To this end, we have tested deep learning techniques based on the U-Net architecture (39).

Vascular network segmentation

A variety of methods were examined for vascular network segmentation. Manual segmentation was carried out using the webknossos user interface (UI). Automatic volume annotation and

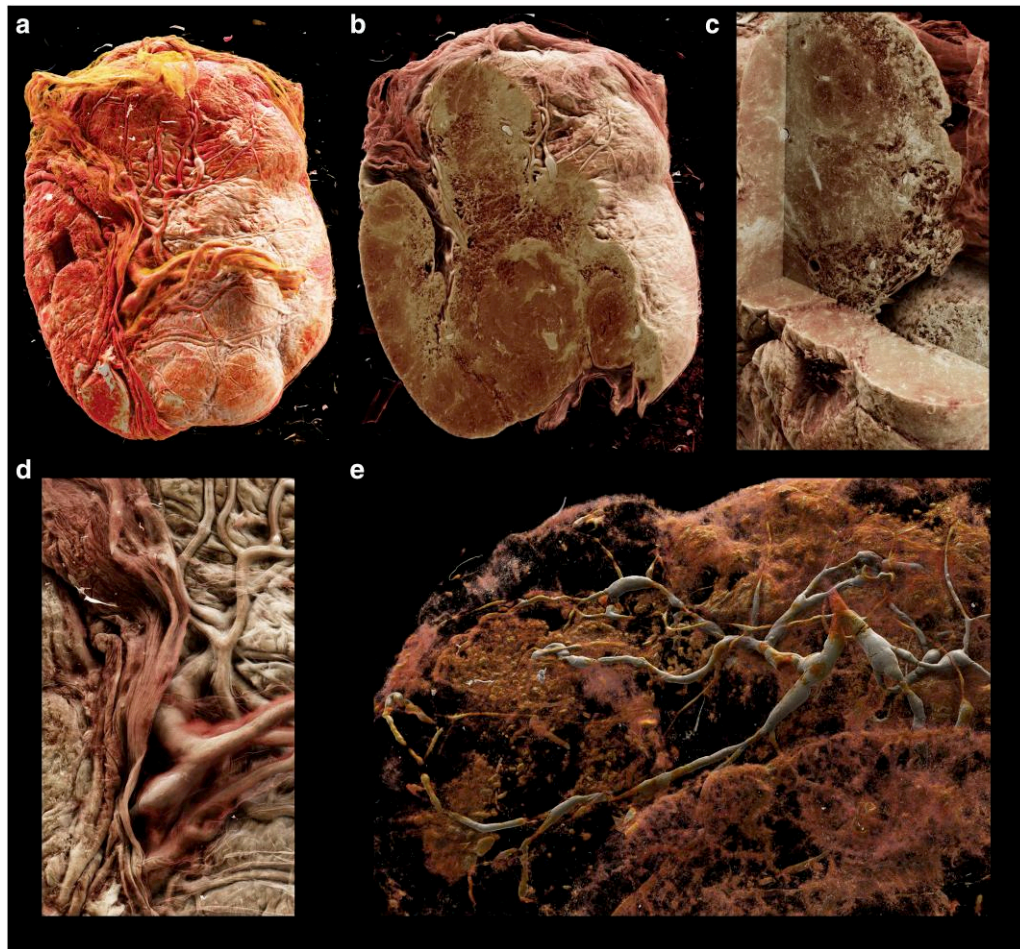


Fig. 4. Cinematic rendering (Cinematic Anatomy, Siemens Healthineers, Germany) of the entire human placenta (Table 1: BM18-T, same placenta as shown in Fig. 2). a) Rendering of entire placenta. At the left, a hole indicates the position from where a biopsy was extracted before the scan. b) Cut through placenta by a vertical plane. High-density structures mostly observed at the surface indicate potential fibrinous tissue regions. c) 3D view inside the maternal side of placental tissue. d) Umbilical cord branches out, creating the vascular network inside the placenta. e) Histogram-based manipulation allows to visualize part of the vascular network with coagulated blood residues (white).

segmentation is facilitated by a machine learning feature based on the ‘Segment Anything Model’ (32). Here, feature branching poses a challenge for automatic segmentation, such that branches need to be segmented separately (see Fig. 5b and Fig. S8 for segmentation results). Automating the segmentation of the entire placenta is essential in view of the significant effort of manual segmentation. This is particularly true when it comes to the segmentation of vasculature in multiple organs within the scope of a clinical study.

To automate the segmentation of the vascular network, a 3D deep learning architecture (V-net) was trained by sparse manual annotations. To this end, a 400 pixel cube volume was extracted from the center of the placenta and the volume was manually annotated using dedicated software (webknossos and micro-sam). This resulted in three labels, namely not annotated voxels (0), placental tissue (1), and vasculature (2). These annotations were used to train the V-net. While at first the sparsity of annotations prevented the validation loss to drop, additional annotations with webknossos as well as training with provided annotations by Tun et al. (40) resulted in a significant improvement of the segmentation results (see Fig. S9 for validation loss plot). The results are highlighted in Fig. S8b. It shows that many small branched segments can be tracked which are otherwise not visible by simple

thresholding. At the same time, larger branches suffer from frequent interruption. The largest challenge is posed by false positives and branch interruptions in smaller branches, resulting in difficulties of 3D visualization and tracing. By simultaneous observation of the falsely segmented regions and annotation of the respective regions with the correct label, network segmentation results can be successively improved. In this study, the focus of the segmentation has been on visualizing vessels. Obtaining segmentations that allow quantification requires significantly more effort.

Translation of HiP-CT to laboratory instrumentation

Beyond the datasets acquired at the BM18 beamline dedicated to human organ imaging, we translated the technique to a laboratory instrumentation. The same sample containers were placed in an μ CT imaging system. The samples were moved close to the detector to obtain large FOV at the expense of magnification (see Table 1: μ CT). The imaging results are shown in Fig. 6. Owing to the flat field being recorded in a 70% EtOH-filled jar, ring and cupping artifacts were significantly reduced. A high contrast can be observed, allowing the identification of tissue substructure and the vascular tree (Fig. 6a). The blood in veins and arteries appears

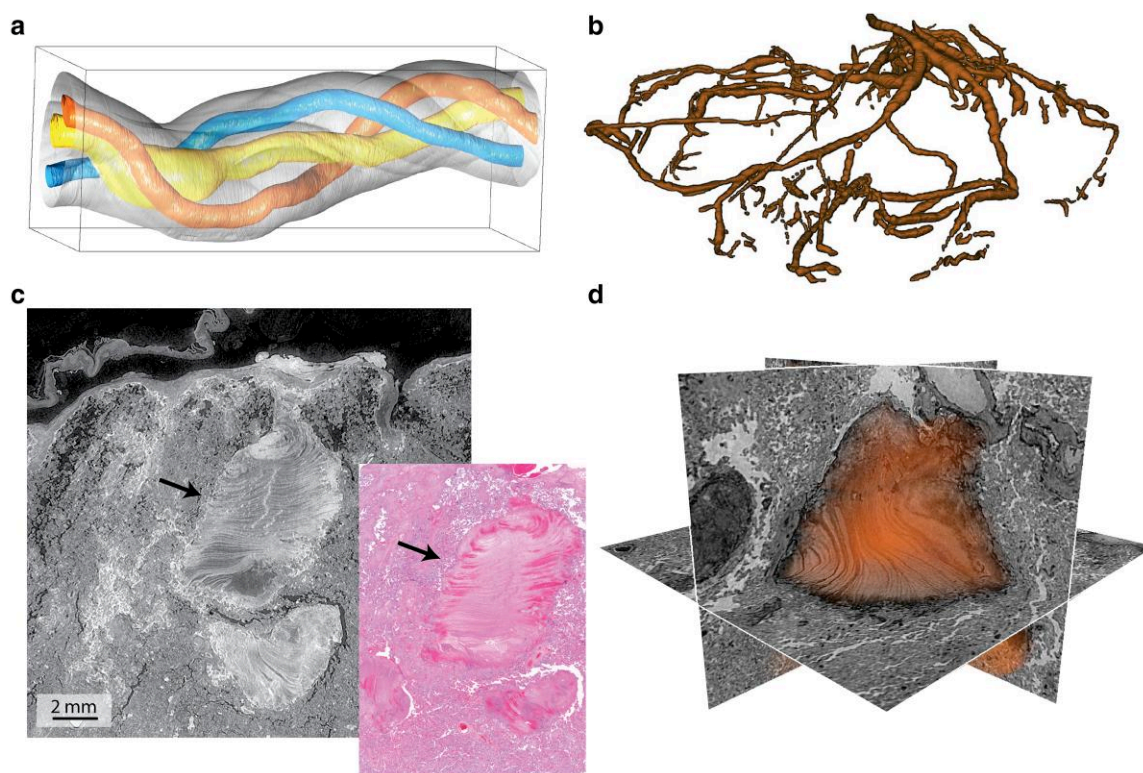


Fig. 5. a) Segmentation of umbilical vein (yellow) and arteries (blue, red) from umbilical cord, same as illustrated in Fig. 2b using the MATLAB nerve-tracking toolbox (41). b) Manual segmentation of a vascular network region using webknossos (30) and skeletonized using FIJI (42). The rendering was created using Avizo 3D. c) Tissue region with intervillous subacute thrombosis in scan of intact human placenta (BM18-T) with clearly distinguishable laminar structured lesions (lines of Zahn). To the right, same region shown in correlative histological slice (a more detailed correlative depiction is shown in Fig. S3). d) Three orthogonal slices with the segmented intervillous thrombus in the center (orange).

to have clotted, resulting in strong attenuation and facilitating segmentation of the broad vasculature segments (Fig. 6b). Contrast variation in the inner placental tissue regions indicate a heterogeneous morphology in terms of tissue density and composition. Cinematic rendering (Fig. 6c) adds to the impression that vasculature can be accurately reconstructed and segmented, allowing for morphometric and geometric analysis of the data.

3D virtual histology with submicron voxel size

Next, we extended the multiscale approach by biopsy extraction and high-resolution scans, using the GINIX instrument dedicated to coherent imaging at beamline P10 of the PETRA III storage ring (DESY, Hamburg). Biopsies with a cross section in the range of 3–5 mm were scanned in different embedding media. Figure S6a,b shows a slice through a 5 mm paraffin-embedded (standard FFPE) sample, where $5 \times 5 \times 3$ (x, y, z) tomograms were recorded and stitched together using the NRStitcher software package. The grid artifact is caused by the overlay of the regions and according superposition of the gray values. Each scan covers ≈ 0.5 cm of placental tissue from a SARS-CoV-2 infected patient at sub- μm voxel sizes ($0.65 \mu\text{m}$). In Fig. 7a,b, results obtained for a biopsy from a control placenta is shown, fixated by 4.5% PFA and liquid embedded in 70% EtOH. Empty beam reference images were recorded with the capillaries with empty solution in the beam, following the concept of the HiP-CT, see Section ‘Methods: Sample preparation’ for details on sample preparation. The results (single tomogram, non-stitched) indicate a superior image quality with regard to SNR and contrast, as well as better tissue preservation compared with the paraffin-embedded sample. The quality of

the scans allows inspection of microvilli and resolves cell nuclei, which can be segmented and counted for the purpose of statistical/morphometric analysis.

Placental villi and fibrin deposition can be distinguished and their presence can be confirmed by correlative light microscopy examination of histological sections (Fig. 8a and Fig. S7). Dark regions visible on the edges in Figs. 9 and 8a,b are identified as aggregates of syncytial nuclei at the interface between terminal villi (syncytial knots). The strong contrast might be caused by accumulation of heterochromatin. The terminal villi have syncytiotrophoblasts on their surface and are filled with villous stroma and fetal capillary vessels. The large visible vessel is surrounded by a thick layer of muscle tissue. An increased number of syncytial knots (Tenny Parker changes) may indicate pregnancy complication e.g. by preeclampsia. Via correlative histology (Fig. 8b), the dark spherical structures were identified as fibroblasts.

For the results presented here, an additional information document is provided, including an overview table (Table S1) of placentas studied, as well as additional figures. These include a comparison of image quality comparison between synchrotron scan (BM18-HR) and in-house scan (μCT -setup), photographs of sample intact placentas and sample preparation, datasets of FFPE human placental tissue acquired at the P10-PB setup, correlative imaging of conventional histology, and the loss curves for the training of the V-net. In addition, we show a cinematic rendering of the fetal side of a healthy human placenta, and of an entire human placenta, and also include a video animation of a rendered healthy human placenta.

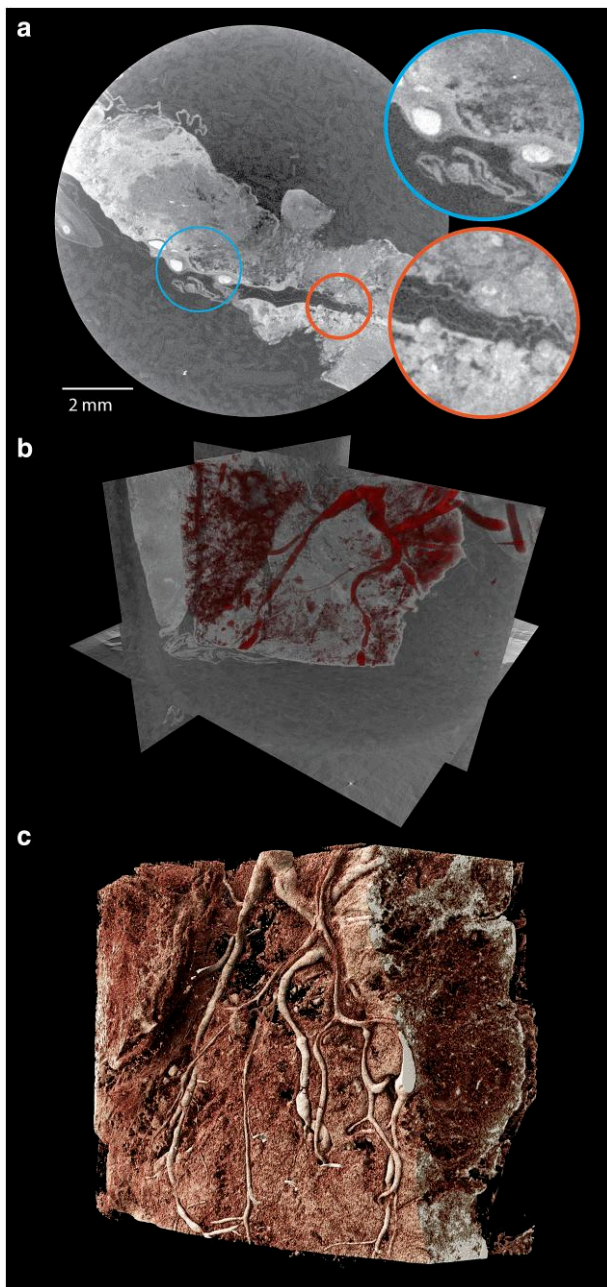


Fig. 6. Laboratory scan of entire healthy human placenta (same placenta as shown in Fig. 2). a) Slice showing placental tissue, reconstructed from a laboratory μ CT scan, with zooms into vasculature and amniotic membrane on the fetal side of the placenta. b) 3D visualization with three orthogonal slices through the volume and rendering of the vascular tree (Avizo 3D, Thermo Fisher Scientific, Waltham, USA). c) Cinematic rendering of the dataset, highlighting the fetal side of the placenta.

Discussion

This work shows an unprecedented view of the 3D tissue organization of an entire human placenta. The main accomplishments of this work are:

- scan of an entire human placenta with a voxel size of $19.9\mu\text{m}$ creating an human placenta atlas, with several high-resolution datasets of particular regions of interest ($\sim 3\mu\text{m}$ voxel size).

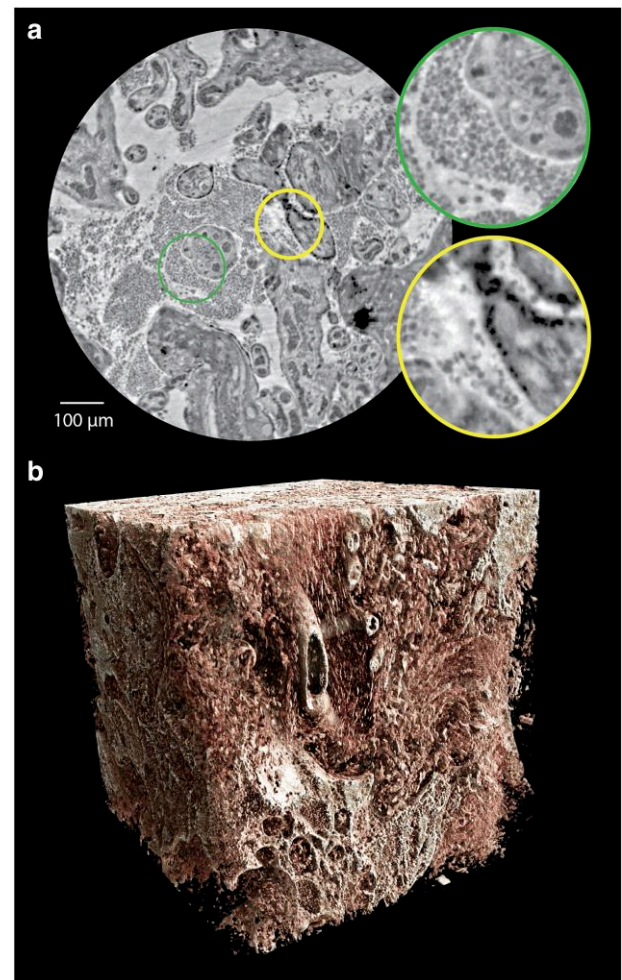


Fig. 7. Synchrotron-recorded data of liquid-embedded samples from P10 coherent applications beamline (DESY, Hamburg) using the P10-PB-setup (Table 1: P10-PB). a) Slice through liquid-embedded (3 mm biopsy punch in 70% EtOH with PBS buffer) tissue sample of healthy placental tissue. b) Cinematic rendering (Cinematic Anatomy, Siemens Healthineers, Germany) of tissue dataset shown in (a).

- first time 3D visualization of placental tissue abnormalities such as an chronic intervillous/subacute thrombi with laminar structured lesions and placental infarcts.
- comparative assessment of placental abnormalities by correlation of the established gold-standard in placental parenchyma analysis—histopathology—to 3D acquired XPCT datasets.
- exploration of 3D image segmentation approaches and quantitative assessment of placental vasculature.
- first achievements in translation of the whole-organ imaging approach (4) from the synchrotron to the laboratory.

The promising novel insights into placenta morphology obtained by the multiscale capability of the presented approach open up a number of opportunities for follow-up investigations. For example, vascular abnormalities occurring in pregnancy complications such as preeclampsia would be an excellent target which could take advantage of the approach. Main future challenges can be identified as:

- adaption of sample preparation protocols to assure a cross-fixation of the entire organ while decreasing the overall preparation time.

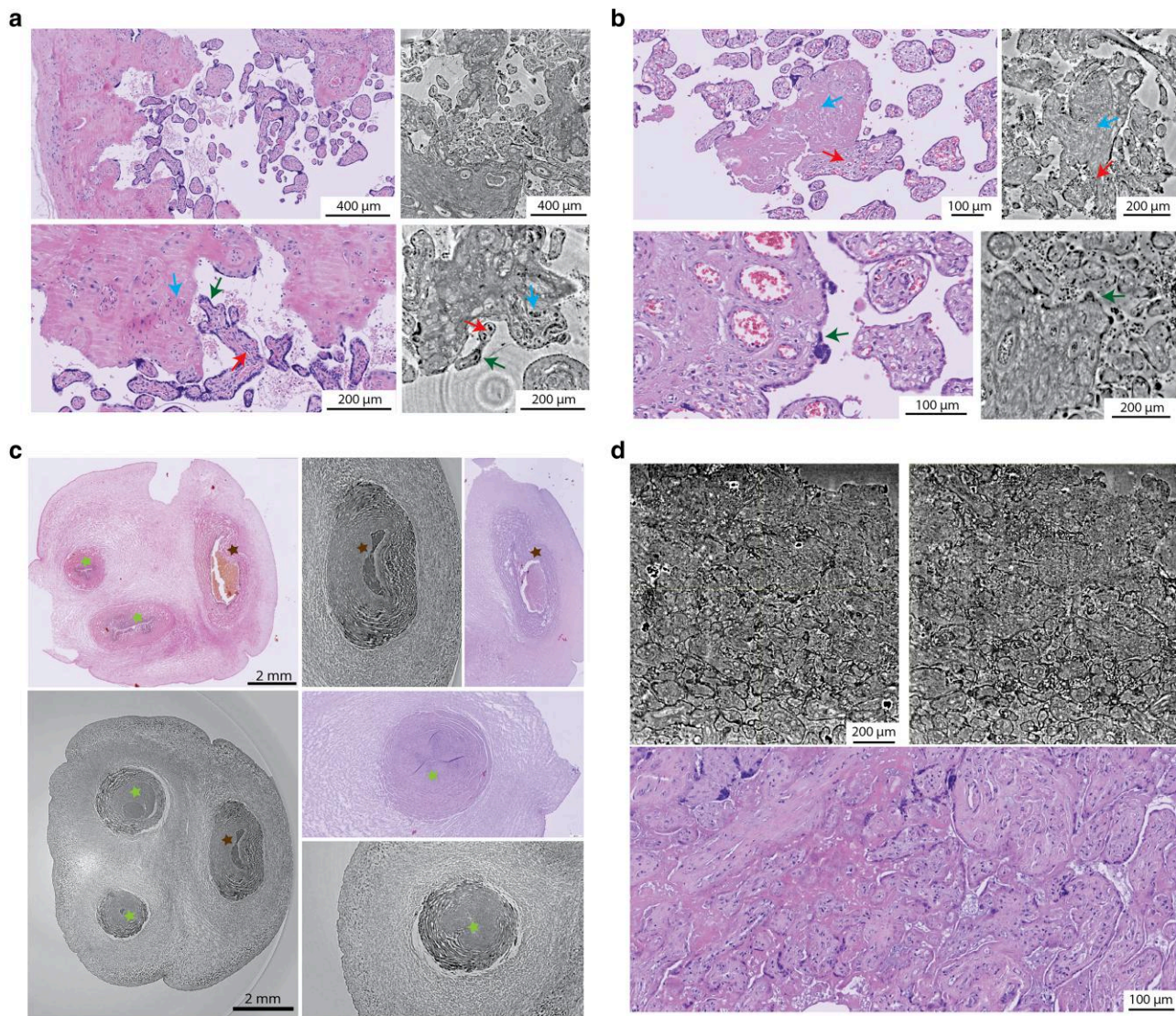


Fig. 8. Correlation of regions of interest of XPCT data and H&E stained histological slices (red arrow denotes vasculature inside placental villi with erythrocytes; blue arrow, fibrin deposition; green arrow, syncytial knots/syncytiotrophoblast). a) Correlative overview on a healthy placenta placental villi (red arrows), intervillous fibrin (blue arrows), and syncytial knots (green arrows). b) Direct comparison of fibrin depositions (top) and syncytial knots (bottom) between histological slices and XPCT-acquired data of placenta with preeclampsia. c) Umbilical cord with two arteries (green asterisk) and one vein (brown asterisk) in healthy placenta Intima, Media, and adventitia are readily visible on XPCT imaging. d) Infarctious regions in XPCT data (top) and histological slices (bottom) recorded in healthy placenta (same sample as Fig. 2).

- contrast enhancement by vessel staining.
- improved segmentation of vascular network using deep learning techniques and topological modeling.
- translation and optimization of the laboratory imaging protocol for whole organs.
- increasing the number of scanned samples including tissue alterations (healthy vs. control) by an automatized high-throughput workflow.

To support the preservation of the sample and to increase the stability, uniform cross-linking of the entire organ with a fixative (such as 4.5% PFA) is required. In this experiment, one week of fixation resulted in only partially cross-linked tissue components, where especially center parts of the placenta remained soft and showed fresh blood residues. Cross-linking duration should therefore be increased for up to a month for entire organs due to the large organ volume and density of tissue organization, alternatively the vascular tree could be perfused with fixative solution to speed up fixation. At the same time, preparation time could

potentially be decreased by organ-specific modification and optimization of the existing protocol (18). In addition, the protocol needs to be re-assessed and optimized with regard to the additional extraction of tissue for 3D histopathological assessment.

To facilitate the segmentation of the vascular tree and morphometric tissue quantification, contrast can be enhanced by perfusion with staining agents (previously explored in (22, 43)). The injection should be administered immediately after the placenta is extracted, and the vascular network should be flushed of any remaining blood beforehand. Potentially candidates which proved suitable for vessel staining in previous XPCT studies include iodine (44–47), gold (48), and neodymium-based (49) staining agents.

As is shown, current imaging capabilities allow to segment the main branches of the vascular tree with semi-manual annotation using dedicated state of the art software packages. We further demonstrate that the manual segmentation can be replaced by implementing a U-Net workflow where only a sub-volume is annotated and a significant part of the vascular tree of the entire

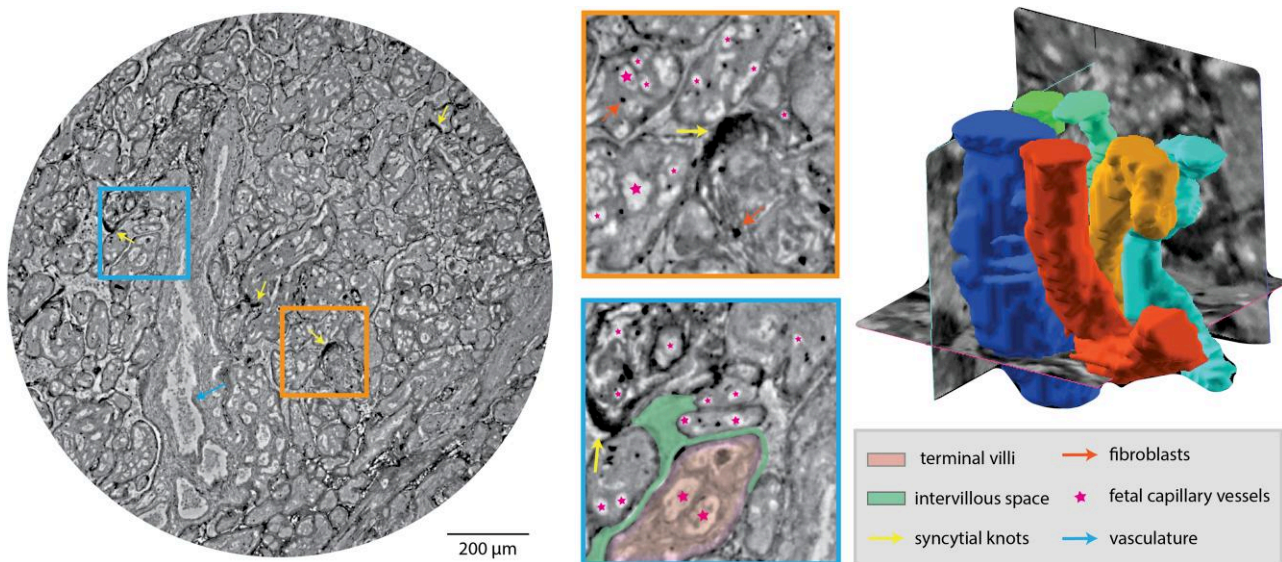


Fig. 9. Synchrotron data (P10-PB setup) from FFPE placental tissue in proximity to an infarctious region, extracted from a physiological placenta. Terminal villi (red) contain fetal capillary vessels (pink star, segmented on the right), are partially surrounded by syncytiotrophoblasts and enclosed by intervillous space (red). We can observe syncytiotrophoblastic (syncytial) knots on the terminal villi surface (yellow arrow) and fibroblasts in the villous stroma (orange arrow).

dataset can be segmented. However, the limited amount of annotated data (serving as ground truth) is a bottle-neck. Advanced vessel segmentation and skeletonization techniques were recently introduced (50–52) and need to be further explored in view of assessment of vascular pathologies. The structure tensor approach should also be tested for further morphometric tissue analysis.

Complementing the synchrotron results, the present work also demonstrates the potential of translating whole organ imaging to laboratory setups and commercially built μ CT scanners. In this way, studies with larger sample numbers (such as demonstrated in (28)) can be realized to investigate morphology-induced functional deficiencies in birth complications such as for example pre-eclampsia. Furthermore, owing to the non-destructive nature of XPCT, smaller volumes can be extracted in targeted ways from the placenta, for subsequent examination with high-resolution instruments as shown in Figs. 7 and 9, as well as for subsequent histological analysis (see infarctious region in Fig. 8d) as is common in clinical practice.

In summary, the presented data demonstrate that X-ray phase-contrast computed tomography (XPCT) of entire organs is a promising technique for studying vascular network connectivity in the human placenta, with a potential to provide new insights into 3D tissue organization and its pathological alterations. In order to assess morphometric features, advanced segmentation techniques need to be applied and appropriate metrics and algorithms for 3D vessel segmentation need to be further explored and developed. The translation of the technique to the laboratory enables the coverage of a statistically significant number of samples, e.g. in context of clinical studies, shedding new light on the etiology of birth complications.

Acknowledgments

We acknowledge assistance in visualization with NVIDIA IndeX (NVIDIA Corporation, USA) and by Klaus Engel with Cinematic Anatomy (Siemens Healthineers, Erlangen, Germany). We thank Susanne Hengst and Eva Campenhausen for help with sample

preparation, Sarah Damerow, Eva Campenhausen, and Jannis Schaeper for support at the beamline, and Markus Osterhoff for implementing the automated stitch recordings at the instrument GINIX/P10 (PETRA III, DESY). We thank Laura Schridde for expert advice in pathology, which was instrumental in the revision. We acknowledge the ESRF for granting beamtime on the BM18 beamline through the proposal MD1373. This experiment was performed using hardware and software tools especially developed for HiP-CT funded by the Chan-Zuckerberg Initiative through a series of grants to the UCL (PI P. Lee). The salaries of H.D. and P.T. are partially funded through these grants.

Supplementary Material

Supplementary material is available at PNAS Nexus online.

Funding

The work was funded by Deutsche Forschungsgemeinschaft (DFG, German Research Foundation)—Project-ID 432680300—SFB 1456/A03 *Mathematics of Experiment* and under Germany's Excellence Strategy—EXC 2067/1-390729940.

Author Contributions

T.S., J.R., and M.F.H. conceived the experiments. M.F.H., C.W., S.M., D.J., M.A., C.W., and A.D. extracted and provided the placenta organs for examination. J.R., A.S., and E.C. conducted sample fixation and preparation. T.S., J.R., P.T., and H.D. conducted the experiments at the BM18 beamline. P.T. and H.D. carried out data processing and volume reconstruction. T.S., J.R., E.C., and A.S. acquired the μ CT and P10 data. P.M.J., A.B.D., V.A.D., and J.R. conducted the deep learning image analysis. J.R. and A.S. annotated the data. T.S., J.R., A.S., S.M., D.J., M.A., A.D., J.G., and M.F.H. interpreted the results. A.D. and S.M. conducted the histological analysis of the sample. J.R. and A.S. worked on rendering and visualization of the data. T.S. and J.R. wrote the manuscript.

Data Availability

The data (reconstructions, segmentations, scripts) are deposited in the open repository Goettingen Research Online (GRO.data) under the link: <https://doi.org/10.25625/18VFLD>. Raw data were generated at ESRF and DESY and will be made public 2 years after the beamtime, which for the ESRF data will be July 2025. Raw data before routine release, or any other additional data/material supporting the findings of this study are available from the corresponding author on request.

References

- Jensen OE, Chernyavsky IL. 2019. Blood flow and transport in the human placenta. *Annu Rev Fluid Mech.* 51(1):25–47.
- Akhavan S, Borna S, Abdollahi A, Shariat M, Zamani N. 2022. Pathologic examination of the placenta and its benefits in treatment plan or follow-up of patients: a cross-sectional study. *Eur J Med Res.* 27(1):Article 113.
- Slator PJ, et al. 2018. Placenta microstructure and microcirculation imaging with diffusion MRI. *Magn Reson Med.* 80(2):756–766.
- Walsh CL, et al. 2021. Imaging intact human organs with local resolution of cellular structures using hierarchical phase-contrast tomography. *Nat Methods.* 18(12):1532–1541.
- Brunet J, et al. 2024. Multidimensional analysis of the adult human heart in health and disease using hierarchical phase-contrast tomography. *Radiology.* 312.
- Rahmani S, et al. 2023. Micro to macro scale analysis of the intact human renal arterial tree with Synchrotron Tomography, biorXiv, <https://www.biorxiv.org/content/10.1101/2023.03.28.534566v1>, preprint: not peer reviewed.
- Kuan AT, et al. 2020. Dense neuronal reconstruction through X-ray holographic nano-tomography. *Nat Neurosci.* 23(12):1637–1643.
- Bosch C, et al. 2024. Non-destructive X-ray tomography of brain tissue ultrastructure, biorXiv, <https://www.biorxiv.org/content/10.1101/2023.11.16.567403v3>, preprint: not peer reviewed.
- Ding Y, et al. 2019. Computational 3D histological phenotyping of whole zebrafish by X-ray histotomography. *Elife.* 8:e44898.
- Dejea H, et al. 2019. Comprehensive analysis of animal models of cardiovascular disease using multiscale X-ray phase contrast tomography. *Sci Rep.* 9(1):Article 6996.
- Saccomano M, et al. 2018. Synchrotron inline phase contrast μ CT enables detailed virtual histology of embedded soft-tissue samples with and without staining. *J Synchrotron Radiat.* 25(4):1153–1161.
- Töpperwien M, van der Meer F, Stadelmann C, Salditt T. 2018. Three-dimensional virtual histology of human cerebellum by X-ray phase-contrast tomography. *Proc Natl Acad Sci U S A.* 115(27):6940–6945.
- Khimchenko A, et al. 2016. Extending two-dimensional histology into the third dimension through conventional micro computed tomography. *Neuroimage.* 139:26–36.
- Khimchenko A, et al. 2018. Hard X-ray nanoholotomography: large-scale, label-free, 3D neuroimaging beyond optical limit. *Adv Sci.* 5(6):Article 1700694.
- Westö C, et al. 2021. Distinct types of plexiform lesions identified by synchrotron-based phase-contrast micro-CT. *Am J Physiol Lung Cell Mol Physiol.* 321:L17–L28.
- Palermo F, et al. 2022. Multilevel X-ray imaging approach to assess the sequential evolution of multi-organ damage in multiple sclerosis. *Commun Phys.* 5(1):Article 290.
- Barbone G, et al. 2022. X-ray multiscale 3D neuroimaging to quantify cellular aging and neurodegeneration postmortem in a model of alzheimer's disease. *Eur J Nucl Med Mol Imaging.* 49(13):4338–4357.
- Brunet J, et al. 2023. Preparation of large biological samples for high-resolution, hierarchical, synchrotron phase-contrast tomography with multimodal imaging compatibility. *Nat Protoc.* 18(5):1441–1461.
- Verleden SE, et al. 2022. From macroscopy to ultrastructure: an integrative approach to pulmonary pathology. *Front Med (Lausanne).* 9:1–7.
- Reichmann J, et al. 2023. Human lung virtual histology by multi-scale x-ray phase-contrast computed tomography. *Phys Med Biol.* 68(11):Article 115014.
- Clercq KD, et al. 2019. High-resolution contrast-enhanced microCT reveals the true three-dimensional morphology of the murine placenta. *Proc Natl Acad Sci U S A.* 116(28):13927–13936.
- Aughwane R, et al. 2019. Micro-CT and histological investigation of the spatial pattern of feto-placental vascular density. *Placenta.* 88:36–43.
- Tun WM, et al. 2021. A massively multi-scale approach to characterizing tissue architecture by synchrotron micro-CT applied to the human placenta. *J R Soc Interface.* 18(179):Article 20210140.
- Junaid TO, Bradley RS, Lewis RM, Aplin JD, Johnstone ED. 2017. Whole organ vascular casting and microCT examination of the human placental vascular tree reveals novel alterations associated with pregnancy disease. *Sci Rep.* 7(1):Article 4144.
- Xian RP, et al. 2024. A closer look at high-energy X-ray-induced bubble formation during soft tissue imaging. *J Synchrotron Radiat.* 31(3):566–577.
- Frohn J, et al. 2020. 3D virtual histology of human pancreatic tissue by multiscale phase-contrast X-ray tomography. *J Synchrotron Radiat.* 27(6):1707–1719.
- Reichardt M, et al. 2021. 3D virtual histopathology of cardiac tissue from covid-19 patients based on phase-contrast X-ray tomography. *Elife.* 10:e71359.
- Reichmann J, et al. 2024. 3D imaging of SARS-CoV-2 infected hamster lungs by X-ray phase contrast tomography enables drug testing. *Sci Rep.* 14(1). <https://doi.org/10.1038/s41598-024-61746-4>.
- Bankhead P, et al. 2017. QuPath: open source software for digital pathology image analysis. *Sci Rep.* 7(1):1–7.
- Boergens KM, et al. 2017. webKnossos: efficient online 3D data annotation for connectomics. *Nat Methods.* 14(7):691–694.
- Archit A, et al. 2023. Segment anything for microscopy, biorXiv, <https://www.biorxiv.org/content/10.1101/2023.08.21.554208v1>, preprint: not peer reviewed.
- Kirillov A, et al. 2023. Segment anything. 2023 IEEE/CVF International Conference on Computer Vision (ICCV); Paris, France. pp. 3992–4003. <https://doi.org/10.1109/ICCV51070.2023.00371>.
- Schindelin J, et al. 2012. Fiji: an open-source platform for biological-image analysis. *Nat Methods.* 9(7):676–682.
- Krause M, Hausherr JM, Burgeth B, Herrmann C, Krenkel W. 2010. Determination of the fibre orientation in composites using the structure tensor and local X-ray transform. *J Mater Sci.* 45(4):888–896.
- Lambin P, et al. 2012. Radiomics: extracting more information from medical images using advanced feature analysis. *Eur J Cancer.* 48(4):441–446.
- Vogel M, Turowski G. *Clinical pathology of the placenta.* De Gruyter, 2019.

- 37 Ackermann M, Jonigk DD. 2022. Microvascular placental alterations in maternal COVID-19. *Am J Obstet Gynecol.* 226(1): 135–136.
- 38 Morotti D, et al. 2021. Molecular pathology analysis of SARS-CoV-2 in syncytiotrophoblast and Hofbauer cells in placenta from a pregnant woman and fetus with COVID-19. *Pathogens.* 10(4):Article 479.
- 39 Ronneberger O, Fischer P, Brox T. 2015. U-net: convolutional networks for biomedical image segmentation. In: Navab N, Hornegger J, Wells WM, AF Frangi, editors. Medical image computing and computer-assisted intervention—MICCAI 2015. Springer International Publishing, Cham. p. 234–241.
- 40 Tun WM. 2021. A massively multi-scale approach to characterizing tissue architecture by synchrotron micro-CT applied to the human placenta. *J R Soc Interface.* 18(179). <https://doi.org/10.1098/rsif.2021.0140>.
- 41 Dahlin LB, et al. 2020. Three-dimensional architecture of human diabetic peripheral nerves revealed by X-ray phase contrast holographic nanotomography. *Sci Rep.* 10(1):Article 7592.
- 42 Lee T-C, Kashyap RL, Chu C-N. 1994. Building skeleton models via 3-D medial surface/axis thinning algorithms. *CVGIP: Graph Models Image Process.* 56(6):462–478.
- 43 Pratt R, et al. 2017. Imaging the human placental microcirculation with micro-focus computed tomography: optimisation of tissue preparation and image acquisition. *Placenta.* 60:36–39.
- 44 Grabherr S, et al. 2008. Angiofil: a novel radio-contrast agent for post-mortem micro-angiography. In: Stock SR, editor. Developments in X-Ray tomography VI, Vol. 7078. SPIE. p. 489–496.
- 45 Heimel P, et al. 2019. Iodine-enhanced micro-CT imaging of soft tissue on the example of peripheral nerve regeneration. *Contrast Media Mol Imaging.* 2019:Article 7483745.
- 46 Gignac PM, et al. 2016. Diffusible iodine-based contrast-enhanced computed tomography (diceCT): an emerging tool for rapid, high-resolution, 3-D imaging of metazoan soft tissues. *J Anat.* 228(6):889–909.
- 47 Gignac PM, Kley NJ. 2018. The utility of DiceCT imaging for high-throughput comparative neuroanatomical studies. *Brain Behav Evol.* 91(3):180–190.
- 48 Hainfeld JF, Slatkin DN, Focella TM, Smilowitz HM. 2006. Gold nanoparticles: a new X-ray contrast agent. *Br J Radiol.* 79(939): 248–253.
- 49 Reichmann J, Ruhwedel T, Möbius W, Salditt T. 2022. Neodymium acetate as a contrast agent for X-ray phase-contrast tomography. *J Med Imaging.* 10(5). <https://doi.org/10.1117/1.JMI.10.5.056001>.
- 50 Tetteh G, et al. 2020. DeepVesselNet: vessel segmentation, centerline prediction, and bifurcation detection in 3-D angiographic volumes. *Front Neurosci.* 14.
- 51 Walsh C, et al. 2024. Reconstructing microvascular network skeletons from 3D images: what is the ground truth? *Comput Biol Med.* 171. <https://doi.org/10.1016/j.combiomed.2024.108140>.
- 52 Yagis E, et al. 2024. Deep learning for 3D vascular segmentation in hierarchical phase contrast tomography: a case study on kidney. *Sci Rep.* 14(1). <https://doi.org/10.1038/s41598-024-77582-5>.